西安交通大学
XI'AN JIAOTONG UNIVERSITY

World Scientific
www.worldscientific.com

Electrical conductivity and vibrational studies induced phase transition in $[N(C_3H_7)_4]_2ZnBr_4$ compound

Souad Chkoundali and Abdelhedi Aydi*

Laboratory of Multifunctional Materials and Applications (LaMMA)
Faculty of Sciences of Sfax, University of Sfax, B.P. 1171, 3000 Sfax, Tunisia

aydi_abdelhedi@yahoo.fr

Bis-Tetrapropylammonium tetrabromozincate was synthesized and characterized by X-ray powder diffraction, as well as vibrational and impedance spectroscopy. Rietveld's refinement of X-ray diffractogram confirmed the crystallization of the compound through the monoclinic system (space group $C_{2/c}$). A temperature study of Raman scattering revealed two phase transitions at approximately $T_1 = 340$ K and $T_2 = 393$ K. The wavenumber and the line width's evolution as a function of temperature showed some peculiarities associated with these transitions, which suggests that they are governed by the reorientation of the organic part $[N(C_3H_7)_4]^+$. The complex impedance plotted as a double semicircular arc in the studied temperature range and the centers of these semicircles lie below the real axis, which indicates that the material is an on-Debye type. These semicircular arcs are related to the bulk and the grain boundary effects. Furthermore, the alternating current conductivity of $[N(C_3H_7)_4]_2ZnBr_4$ obeyed Jonscher's law: $\sigma_{AC}(\omega) = \sigma_{dc} + A\omega^s$ and the conduction could be attributed to the correlated barrier hopping (CBH) model in both region(I) and (II) and the Non-overlapping Small Polaron Tunneling (NSPT) in region (III).

Keywords: Bis-Tetrapropylammonium tetrabromozincate; Raman spectroscopy; phase transition; electrical conductivity; conduction mechanism.

1. Introduction

In recent years, phase transition hybrid organic–inorganic materials have drawn the attention and whetted the interest of numerous scientists owing to the fact that they exhibit promising potential applications in data storage, optoelectronic devices and other fields.[1,2] Compared to traditional inorganic materials or organic materials, organic–inorganic phase transition compounds combine the prominent characteristics of both organic and inorganic parts within a single molecule, showing more advantages, such as structural diversity, simple synthesis, adjustable structures and environment friendly.[3–6]

Multiple prior works argue that organic ammonium cations are the outstanding constructional units for the order–disorder phase transition materials. Resting on this strategy, a great number of phase transition compounds with ammonium cations have been investigated in recent years. For instance, dimethylammonium, tetramethylammonium and tetrapropylammonium, which possess small-volume and conformational flexible.[7]

Hybrids compounds of the general formula A_2MX_4, where A is the alkyl ammonium group, M stands for a divalent metal and X corresponds to a halogen, have been largely studied.[8–10] As an element of this group, we opted to examine $[N(C_3H_7)_4]_2ZnBr_4$ compound material for a deeper investigation. It crystallizes in the monoclinic system ($C_{2/C}$ space group).[11] The atomic arrangement is described by an alternation of organic and inorganic layers in the [1 0 0] direction, which consists of $[N(C_3H_7)_4]^+$ and $[ZnBr_4]^{2-}$ groups (Fig. 1).

As an extension of our concern with the Bis-Tetrapropylammonium tetrabromozincate compounds, Raman scattering and electrical properties are explored in order to investigate the phase transition of this compound.

2. Experimental Procedure

Organic–inorganic hybrid compound, $[N(C_3H_7)_4]_2 [ZnBr_4]$, has been successfully synthesized at room temperature by slow evaporation according to a process which has already been detailed in the literature.[11]

The phase purity and homogeneity of the $[N(C_3H_7)_4]_2ZnBr_4$ compound were verified using X-ray powder diffraction analysis. Using a Phillips PW 1710 powder diffractometer operating with CuK_α ($\lambda = 1.5405$ Å), the pattern of the X-ray diffraction was recorded in a wide range of Bragg angles ($9° < 2\theta < 50°$).

The Raman scattering spectra were determined using a Horiba–Jobin–Yvon T64000 Raman spectrometer in the frequency range of 100–3200 cm⁻¹ through the use of the 514.5 nm radiation of an Ar/Kr laser as excitation. These analyses were performed, as a function of temperature, in a Linkam heating stage up to 415 K.
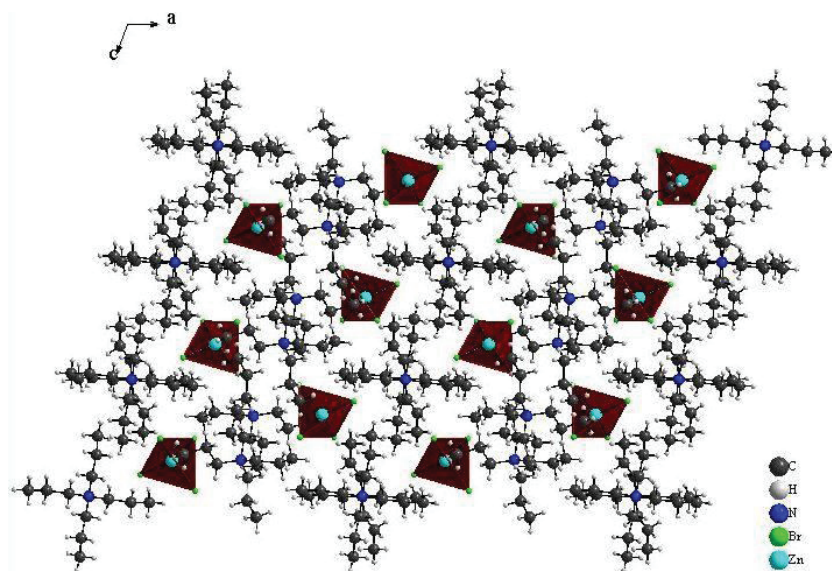
---

*Corresponding author.

Fig. 1.   Crystal structure of the [N(C₃H₇)₄]₂ZnBr₄, view along the *b* axis.

The wavenumber and the width of Raman lines were specified using LabSpec5 software with a combined Lorentzian–Gaussian band shape for the fitting procedure.

To study the electrical properties of the $[N(C_3H_7)_4]_2ZnBr_4$ compound, the crystals were ground into a fine powder then pressed into a cylindrical pellet of 8 mm in diameter and 1.1 mm in thickness using 3 t/cm uniaxial pressure. The measurements were carried out in the frequency and temperature range of 200–5 MHz and 303–423 K, respectively, using a HP4284 impedance analyzer.

3.   Results and Discussion

3.1.   *X-ray powder diffraction*

The X-ray diffraction pattern of the $[N(C_3H_7)_4]_2ZnBr_4$ compound at room temperature is depicted in Fig. 2. The Rietveld refinement was conducted using the FULLPROF software Program. The circles stand for experimental data and the line corresponds to the simulated pattern. The purity of the studied compound was confirmed and the reflection peaks were indexed in the monoclinic system ($C_{2/C}$ space group). The refined cell parameters proved to be as follows: $a = 33.132\ (5)$ Å, $b = 14.234\ (3)$ Å, $c = 15.081\ (2)$ Å and $\beta = 110.23(1)°$. These parameters go in good agreement with those reported in this literature.[11] The quality of the refinement was evaluated through the goodness of Fit $\chi^2 = 6.67$. The values of the reliability factors obtained from the refinement are $R_{\omega p} = 8.99$, $R_p = 8.15$ and $R_{exp} = 3.48$.

3.2.   *Temperature evolution of Raman spectra*

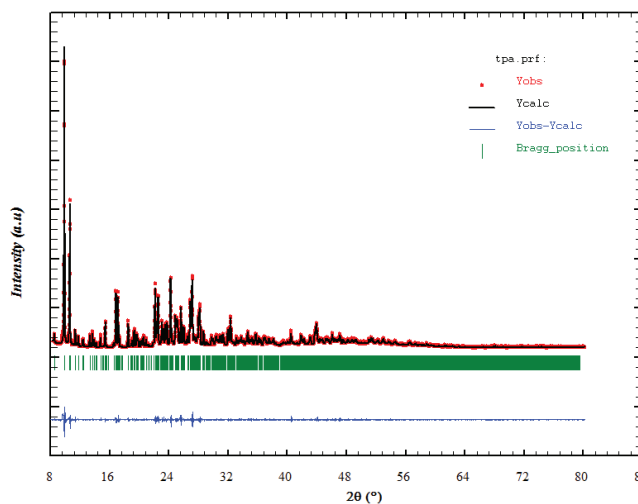The strong Raman bands observed in the 2988–2905 cm⁻¹, are assigned to the stretching vibrations of the CH₃ and CH₂

Fig. 2.   X-ray powder diffraction pattern for [N(C₃H₇)₄]₂ZnBr₄ compound.

groups while the bands between 1460 cm⁻¹ and 1350 cm⁻¹ are attributed, respectively, to the asymmetric and symmetric bending vibration of the CH₃ group. As for the bands observed in the spectral range 847–750 cm⁻¹, they emanate from the bending of the (C–C–C + C–N–C) groups and the N–C stretching vibrations. However, the internal modes of ZnBr₄ anion are below 312 cm⁻¹. In fact, the assignments of the observed bands are established by comparing them to similar compounds, such as [N(C₃H₇)₄]₂SbCl₄,[12] [N(C₃H₇)₄]₂CoCl₄,[13] [N(C₃H₇)₄]₂SnCl₆,[14] [N(C₃H₇)₄]₂FeCl₄,[15] [(C₃H₇)₄N][M(N(CN)₂)₃],[16] and [(C₃H₇)₄N][Cd(N(CN)₂)₃] compounds.[17] These vibrational wavenumbers together with the proposed band assignments are outlined in Table 1.

Table 1. Assignments of the most important observed bands in Raman spectra of $[N(C_3H_7)_4]_2ZnBr_4$ at room temperature.

Intensity Raman (cm⁻¹)	Assignements
164	ν_1 (ZnBr)
193	ν_3 (ZnBr)
312	ν_1 (ZnBr)
334	ρ_r (CH$_2$)
368	δ(NC$_4$) + δ (C–C–C)
513	δ(NC$_4$) + δ (C–C–C)
750	ν_2 (NC$_4$)
780	ν_1 (NC$_4$)
847	δ_s(C–C–C) + δ_s(C–N–C)
872	δ_s(C–C–C) + δ_s(C–N–C)
918	ν_s (NC)
937	δ(C–N–C)
972	δ(C–N–C)
1031	ρ_r (CH$_3$) + ρ_r (CH$_2$)
1100	δ (Skeletel)
1134	δ (Skeletel)
1151	t(CH$_2$)
1316	ω (CH$_2$)
1330	δ_s(CH$_3$)
1350	δ_s(CH$_3$)
1448	δ_{as}(CH$_3$)
1460	δ_{as}(CH$_3$)
2741	—
2877	ν_s(CH$_2$)
2905	ν_s(CH$_2$)
2934	ν_{as} (CH$_2$)
2955	ν_{as}(CH$_2$)
2970	ν_{as} (CH$_3$)
2988	ν_{as} (CH$_3$)

Note: ν_s, symmetric stretching; ν_{as}, asymmetric stretching; δ_{as}, asymmetric bending; ω, wagging; t, twisting; δ, bending and ρ_r, rocking.

The intrinsic goal of this work is to find the sensitive modes for the phase transition at $T_1 = 340$ K and $T_2 = 393$ K in the $[N(C_3H_7)_4]_2ZnBr_4$ compound. Raman spectra, at several temperatures, are illustrated in Figs. 3(a)–3(d). These spectra are devised into four domains: the first from 100 cm⁻¹ to 320 cm⁻¹, the second from 320 cm⁻¹ to 1000 cm⁻¹, the third from 1000 cm⁻¹ to 1600 cm⁻¹ and the fourth from 2600 cm⁻¹ to 3200 cm⁻¹. Several Raman mode wavenumbers change discontinuously around the temperatures of phase transition evidenced at $T_1 = 340$ K and $T_2 = 393$ K by DSC

measurements.[11] A careful analysis of these spectra clearly portrays that the results and discussion of the shape of most bands, obtained between 100 cm⁻¹ and 320 cm⁻¹, where the anionic part is found, do not change a lot below the phase transition temperatures (T_1 and T_2), which is indicative that these modes are not directly connected to the phase transitions. However, several bands displayed a significant shift in their frequency position and half-width assigned to the internal vibrations of the $[(C_3H_7)_4N]^+$ cation. The position and width at half maximum for the selected lines, obtained between 320 cm⁻¹ and 1600 cm⁻¹, are depicted in Figs. 4(a) and 4(b). The band related to the temperature dependence of the rocking vibration (ρ_r (CH$_2$)) located at 334 cm⁻¹, presented a variation in its position to the low wavenumber by 2 cm⁻¹ around the first transition (T_1) and to the high wavenumber by 4 cm⁻¹ around the second transition (T_2). Half-width decreased by 7 cm⁻¹ before the first transition (T_1) and by 6 cm⁻¹ after the second transition (T_2). The peak observed at 780 cm⁻¹ is assigned to the symmetric stretching vibration of ν_1(NC$_4$) which decreased by 3 cm⁻¹ and half-width increased by 12 cm⁻¹ before the second transition. The wavenumber of bands located at 872 cm⁻¹ and 847 cm⁻¹, which are attributed, respectively, to the (δ_s(CH$_3$) + δ_s(CH$_2$)) and (δ_s(C–N–C) + δ_s(C–C–C)), is decreased by 3 cm⁻¹ around T_2. Obviously, the band, located at 1350 cm⁻¹ and assigned to the symmetric bending vibration of δ_s(CH$_3$), vanished above the second transition (T_2). The anti-symmetric bending vibration of δ_{as}(CH$_3$)) observed at 1460 cm⁻¹, presented a variation in the position by 9 cm⁻¹, while the half-widths increased by 10 cm⁻¹ at T_2.

The temperature dependence of Raman spectra in the region of the stretching symmetric and asymmetric vibrations between 2600 cm⁻¹ and 3200 cm⁻¹ is reported in Figs. 5(a) and 5(b). The band at 2905 cm⁻¹ related to the symmetric stretching ν_s(CH$_2$) mode, shifted a higher wavenumber by 4 cm⁻¹ with a significant jump in the half-width at the second transition (T_2). The anti-symmetric stretching vibration of ν_{as}(CH$_2$), observed at 2934 cm⁻¹, presented a position variation by 3 cm⁻¹; while the half-widths increased by 8 cm⁻¹ at T_2. The band at 2955 cm⁻¹ associated with the asymmetric stretching vibration of ν_{as}(CH$_2$) vanished above the second transition (T_2).

The last band related to the temperature dependence of asymmetric stretching vibration ν_{as}(CH$_3$), located at 2970 cm⁻¹, shows a variation in its position to the high wavenumber by 2 cm⁻¹ at T_1 and 4 cm⁻¹ at T_2, and in its half-width by 5 cm⁻¹ around T_2.

The significant changes in the Raman spectra are observed at $T_2 = 393$ K for some internal modes of cationic parts, which is suggestive that the dynamics of the $[N(C_3H_7)_4]^+$ cationic parts evidence the contribution of the mechanism of phase transition.[18] In order to verify that the phase transitions are correlated with changes in the dynamical state of the cationic groups, a quantitative study about the band located at 2970 cm⁻¹ (ν_{as}(CH$_3$)) was accomplished.
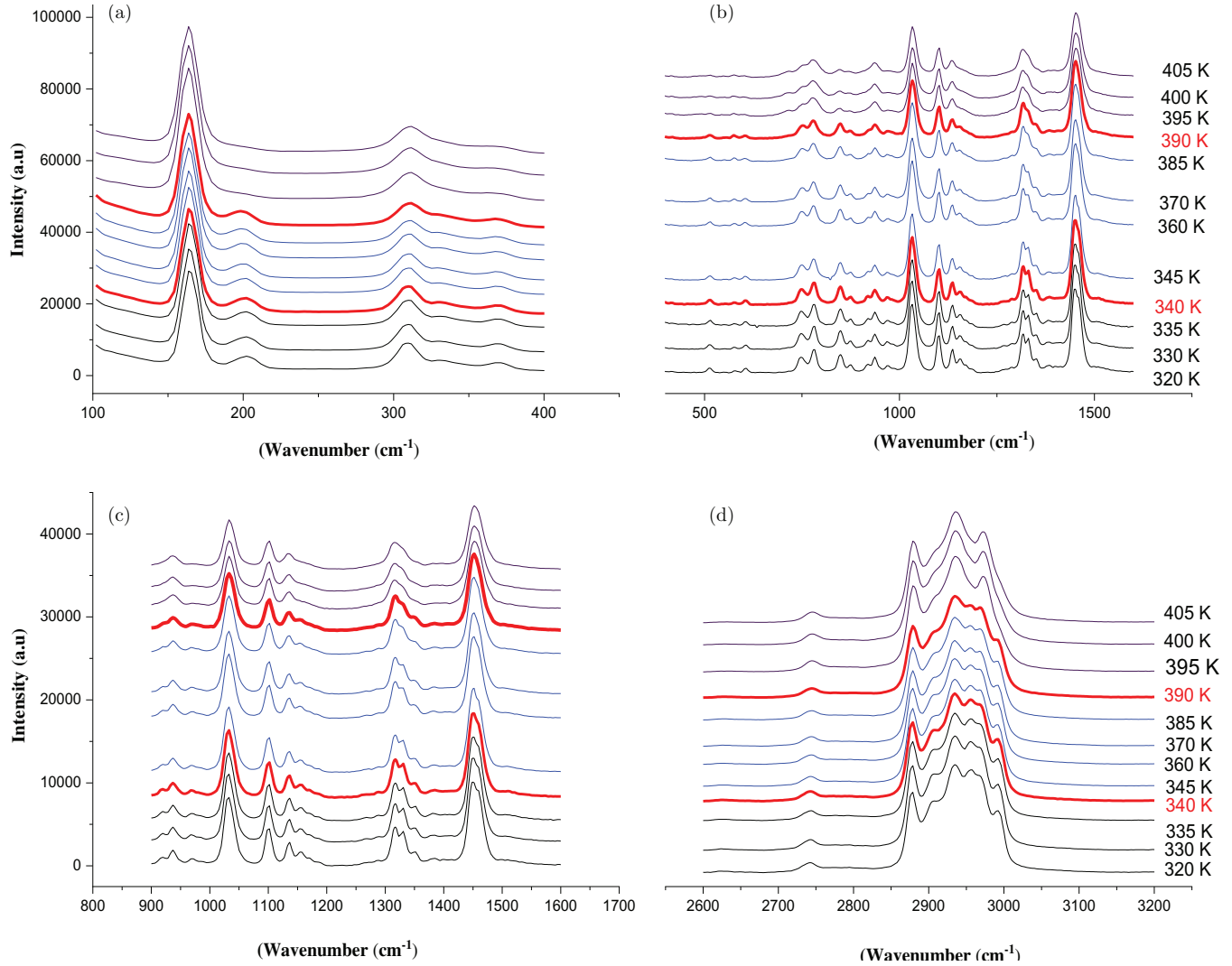
Fig. 3. Evolution of the Raman spectrum as a function of temperature: (a) from 100 cm^{-1} to 320 cm^{-1}, (b) from 320 cm^{-1} to 1000 cm^{-1}, (c) from 1000 cm^{-1} to 1600 cm^{-1} and (d) 2600–3200 cm^{-1}.

3.3. Temperature dependence of the wavenumber

The temperature dependence of Raman wavenumber of a phonon connected to an order–disorder mechanism according to Andrade and Porto[19] is expressed in terms of

$$\nu^2 = \nu_0^2 \left[1 + \gamma(T - T_c)\right], \tag{1}$$

where γ is the thermal coefficient and ν_0 is the "hard-core wavenumber" at temperature transition (T_{tr}). Generally, the values of γ are so small that we can approximate by the following equation[20]:

$$\nu = \nu_0 \left[1 + \frac{\gamma}{2}(T - T_c)\right]. \tag{2}$$

The thermal coefficient depends on the variation of the wavenumber position and the volume of the crystal according to the following expression:

$$\gamma_i = -\frac{\Delta\nu_i}{\nu_i} * \frac{V}{\Delta V}, \tag{3}$$

where ΔV and $\Delta\nu_i$ are the variations of the volume as well as of the wavenumber position, respectively. V corresponds to the original volume and ν_i stands for the band position of the mode at room temperature.

Relying on the approximation of Gruneisen, the relative change of any vibration is directly proportional to the relative change in the volume.[21] Figure 6 discloses the dependency of Raman wavenumber versus temperature of the analyzed band at 2970 cm^{-1} fitted using Eq. (2). We obtained the expansion coefficient $\gamma = 5.12 \cdot 10^{-3}$ K^{-1} for $T < T_1$, $\gamma = 5.08 \cdot 10^{-3}$ K^{-1} for $T_1 < T < T_2$ and $\gamma = 5 \ 10^{-3}$ K^{-1} for $T > T_2$. Hence, the decrease of the thermal coefficient related to the changes of the wavenumber position indicates an increase of the cell volume due to a structural transformation. Indeed, an
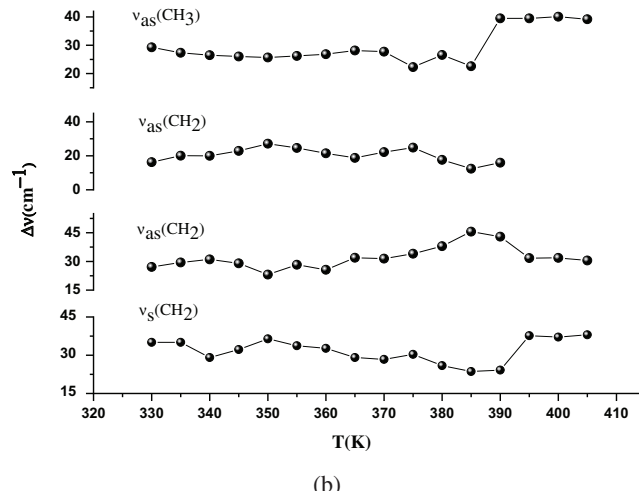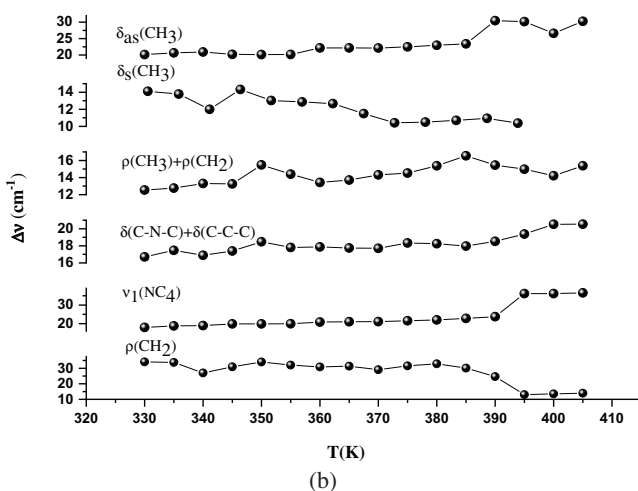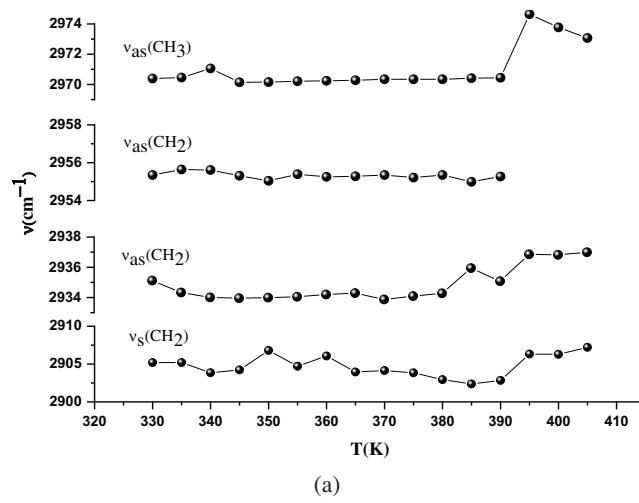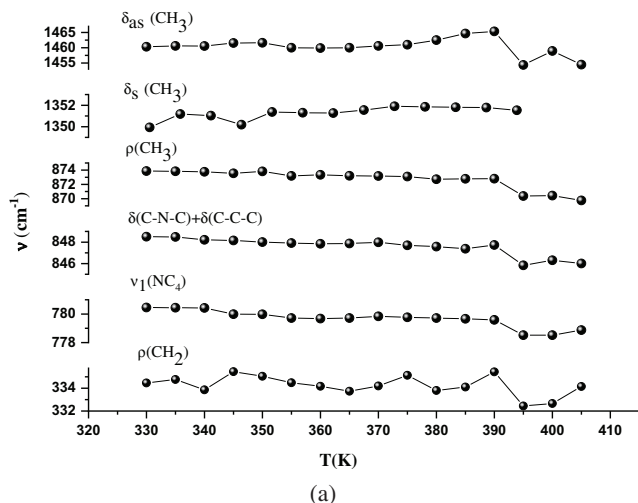
Fig. 4.   Evolution of certain positions Raman (a) and (b) width at mid-height as a function of temperature in the region 320–1600 cm^{-1}.

Fig. 5.   Evolution of certain positions Raman (a) and (b) width at mid-height as a function of temperature in the region 2600–3200 cm^{-1}.

important weakening of the Van Der Waals interaction and the CH$_3$ groups involved in the C–H Br Van Der Waals interaction gain motional freedom.[22]

3.4. *Temperature dependence of the full width of half maximum*

To check whether the phase transitions are correlated with changes of the [N(C$_3$H$_7$)$_4$]$^+$ groups, we followed the analysis of the full width at half maximum (FWHM), which is based on the theory used for the damping associated with an order–disorder mechanism. The analysis of the FWHM, described by Carabatos–Nedelec and Becker, was undertaken.[23] The temperature dependence of the band-width is described as follows[24]:

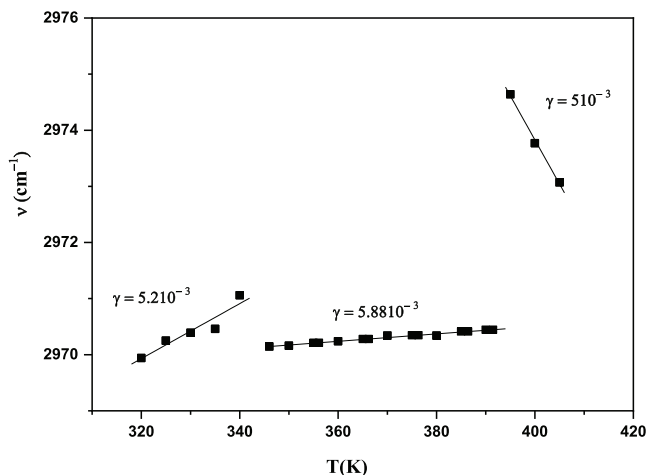$$\Gamma(\omega) = (a + bT) + c\frac{\tau_c}{1 + \omega^2\tau_c^2}, \qquad (4)$$

Fig. 6.   Temperature dependence of the band position at 2970 cm^{-1}.

where $1 <<< (\omega\tau_c)^2$, ω is the phonon wavenumber and τ_c is the mean reorientational time of the atoms to jump from one potential to another. It is provided as follows:

$$\tau_c = \tau_0 \exp\left(\frac{E_a}{k_B T}\right), \tag{5}$$

where E_a is the activation energy for the mode connected to the order/disorder transition, k_B is the Boltzman constant and τ_0 is the relaxation time at infinite temperature. Equation (4) can then be written as follows:

$$\text{FWHM}(T) = (a + bT) + c\exp\left(\frac{E_a}{k_B T}\right). \tag{6}$$

The linear part of Eq. (6) corresponds to the vibrational relaxation and the exponential term stands for the reorientational relaxation. The latter is connected to the thermal molecular reorientational motions of a diffusive nature.

The thermal variation of FWHM pertaining to the band located at 2970 cm^{-1} ($\nu_{as}(CH_3)$), is plotted in Fig. 7. The activation energies obtained by fitting with Eq. (6) are: $E_{a1} = 112$ kJ mol^{-1} in region I, $E_{a2} = 110$ kJ mol^{-1} in region II and $E_{a3} = 88$ kJ mol^{-1} in region III. In fact, the decrease of activation energy refers probably to the decrease of the population involved in this vibration, which can be due to the change of the conformation of the $[N(C_3 \cdot H_7)^+]$ cation.[7]

3.5. *Impedance studies*

Impedance spectroscopy is regarded as the most reliable technique designed to investigate the electrical properties and processes of materials. It provides a direct correlation between the response of a real system and an idealized model circuit composed of discrete electrical components.[25]
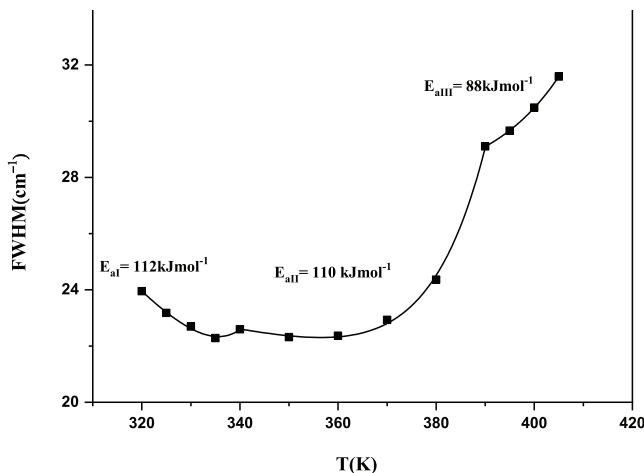

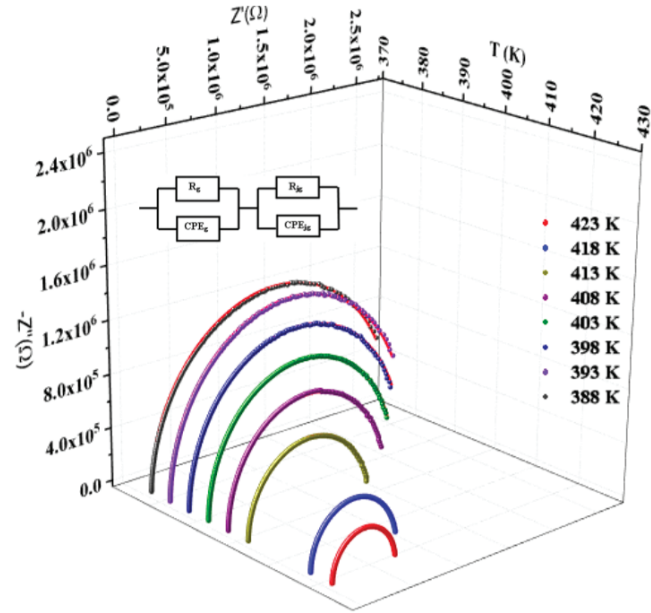Fig. 7. Temperature dependence of the band half-widths at 2970 cm^{-1}.

Fig. 8. Complex impedance plots at different temperatures of $[N(C_3H_7)_4]_2ZnBr_4$ compound.

The complex impedance data ($-Z''$ versus Z'), of $[N(C_3H_7)_4]_2ZnBr_4$ compound for some representative temperatures, are shown in Fig. 8. All these plots are formed by two semi-circles. Thus, the lower frequency dispersion is associated with the grain boundary and the higher one relates to the interior grain.[26] In other words, the centers of semi circles, that compose the total electric response, are centered below the real axis (Z). The latter confirms the presence of non-Debye type of relaxation in materials. The impedance data are fitted to an equivalent circuit model consisting of two parallel R-CPE circuits connected in series (inset Fig. 8).

The impedance of the constant phase element (Z_{CPE}) is given by the following equation:[27]

$$Z_{CPE} = \frac{1}{Q(j\omega)^{\alpha}}, \tag{7}$$

where Q indicates the value of the capacitance of the CPE element and α represents the degree of deviation with respect to the value of the pure capacitor.

The real and imaginary components of the whole impedance were calculated according to the following expressions:

$$Z' = \frac{R_g^2 Q_1 \omega^{\alpha_1} \cos(\alpha_1 \pi / 2) + R_g}{(1 + R_g Q_1 \omega^{\alpha_1} \cos(\alpha_1 \pi / 2))^2 + (R_g Q_1 \omega^{\alpha_1} \sin(\alpha_1 \pi / 2))^2}$$
$$+ \frac{R_{gb}^2 Q_2 \omega^{\alpha_2} \cos(\alpha_2 \pi / 2) + R_{gb}}{(1 + R_{gb} Q_2 \omega^{\alpha} \cos(\alpha_2 \pi / 2))^2 + (R_{gb} Q_2 \omega^{\alpha_2} \sin(\alpha_2 \pi / 2))^2}, \tag{8}$$

$$-Z'' = \frac{R_g^2 Q_1 \omega^{\alpha_1} \sin(\alpha_1 \pi / 2)}{(1 + R_g Q_1 \omega^{\alpha_1} \cos(\alpha_1 \pi / 2))^2 + (R_g Q_1 \omega^{\alpha_1} \sin(\alpha_1 \pi / 2))^2}$$

$$+ \frac{R_{gb}^2 Q_2 \omega^{\alpha_2} \sin(\alpha_2 \pi / 2)}{(1 + R_{gb} Q_2 \omega^{\alpha_2} \cos(\alpha_2 \pi / 2))^2 + (R_{gb} Q_2 \omega^{\alpha_2} \sin(\alpha_2 \pi / 2))^2}. \tag{9}$$

The refinement results performed using the selected electrical model are summarized in Table 2. Let (R_g, R_{jg}) and (Q_g, Q_{jg}) be the resistance and capacitance of the CPE element of grains and grain boundaries, respectively, whereas α $(0 < \alpha < 1)$ is the fractal exponent.

In order to check the choice of the equivalent circuit, we present in Figs. 9(a) and 9(b) the variations of the experimental values of Z′ and Z″ at some temperatures versus the simulated ones calculated using the parameters extracted from the equivalent circuit. Departing from figure, it is quite obvious that the slope obtained from the linear fit of these curves at each temperature is substantially equal to the unity. The good consistency between the experimental and theoretical data implies that the used equivalent circuit describes reasonably well the electric properties of Bis-Tetrapropylammonium tetrabromozincate sample.

The continuous current (dc) conductivity from the grain contribution can be determined from the following expression:

$$\sigma g = \frac{e}{S * R_g}, \tag{10}$$

where e and S are, respectively, the thickness and the area of the pellet.

The thermal evolution of the bulk conductivity is shown in Fig. 10. It was observed that σ_g increases with the increase of temperature and follows the Arrhenius behavior, which is given as follows:

$$\sigma_b = \sigma_0 \exp\left(-\frac{E_a}{K_B T}\right), \tag{11}$$

where E_a is the activation energy, A is the pre-exponential factor and k_B is the Boltzmann's constant.

All phase transitions appearing in the Raman spectroscopy are affirmed by the change of the curve slope at T_1 and T_2. The values of the activation energy determined from the linear adjustment to the data points are $E_{a(I)} = 0.38$ eV in region I, $E_{a(II)} = 0.61$ eV in region II and $E_{a(III)} = 0.44$ eV in

Table 2. The equivalent circuit parameters for the $[N(C_3H_7)_4]_2ZnBr_4$ compound.

| T (K)	R_g (Ω)	Q_g (10^{-10} F)	α_g	R_{gb} (Ω)	Q_{gb} (10^{-8} F)	α_{gb}
323	$5.21 \cdot 10^7$	3.073	0.98615	$1.73 \cdot 10^6$	0.13	0.91154
328	$4.49 \cdot 10^7$	2.74	0.98163	$9.86 \cdot 10^5$	0.18	0.90218
333	$3.89 \cdot 10^7$	2.93	0.97727	$8.90 \cdot 10^5$	0.18	0.90449
338	$2.92 \cdot 10^7$	2.50	0.98782	$8.72 \cdot 10^5$	0.17	0.90344
343	$2.25 \cdot 10^7$	2.30	0.99063	$8.43 \cdot 10^5$	0.13	0.91814
348	$1.71 \cdot 10^7$	2.54	0.98819	$8.20 \cdot 10^5$	0.15	0.91185
353	$1.04 \cdot 10^7$	2.78	0.9873	$7.69 \cdot 10^5$	0.09	0.94116
358	$9.21 \cdot 10^6$	2.71	0.9837	$6.69 \cdot 10^5$	0.19	0.89855
363	$7.53 \cdot 10^6$	2.63	0.98109	$6.48 \cdot 10^5$	0.11	0.93779
368	$6.46 \cdot 10^6$	3.05	0.9519	$5.70 \cdot 10^5$	0.07	0.99404
373	$4.85 \cdot 10^6$	2.81	0.94409	$1.73 \cdot 10^5$	0.11	0.99684
378	$3.65 \cdot 10^6$	2.78	0.94277	$1.50 \cdot 10^5$	0.17	0.98157
383	$2.77 \cdot 10^6$	2.39	0.96419	$1.29 \cdot 10^5$	0.24	0.95479
388	$2.60 \cdot 10^6$	1.97	0.96794	$2.94 \cdot 10^4$	2.57	0.91165
393	$2.50 \cdot 10^6$	1.59	0.98846	$2.01 \cdot 10^4$	3.80	0.73856
398	$2.21 \cdot 10^6$	1.45	0.99522	$1.37 \cdot 10^4$	3.56	0.9023
403	$1.90 \cdot 10^6$	1.41	1.00044	$4.21 \cdot 10^3$	4.81	0.99103
408	$1.61 \cdot 10^6$	1.40	0.99783	$3.85 \cdot 10^3$	6.40	0.74712
413	$1.22 \cdot 10^6$	1.51	0.98826	$2.79 \cdot 10^3$	6.53	0.71726
418	$8.31 \cdot 10^5$	1.42	0.99568	$2.23 \cdot 10^3$	5.06	0.78589
423	$6.14 \cdot 10^5$	1.40	0.99699	$1.07 \cdot 10^3$	3.28	0.84235

(a)

(b)
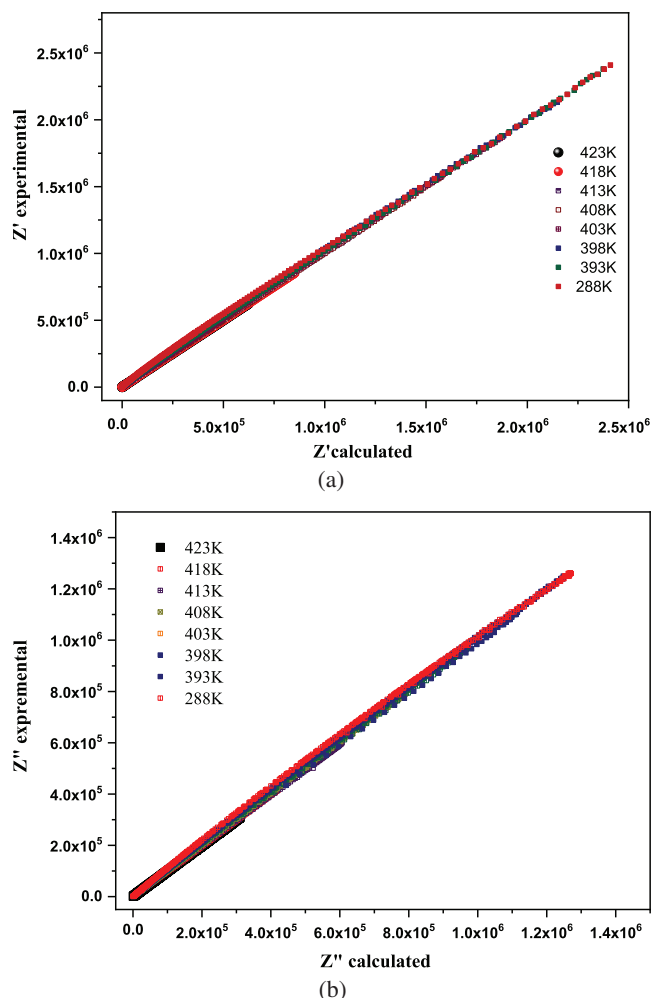
Fig. 9.   (a) Measured and calculated values of the real part of the complex impedance. (b) Measured and calculated values of imaginary part Z''.
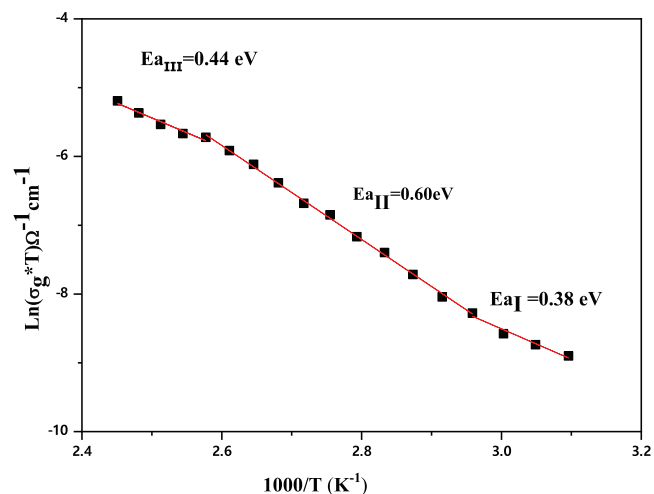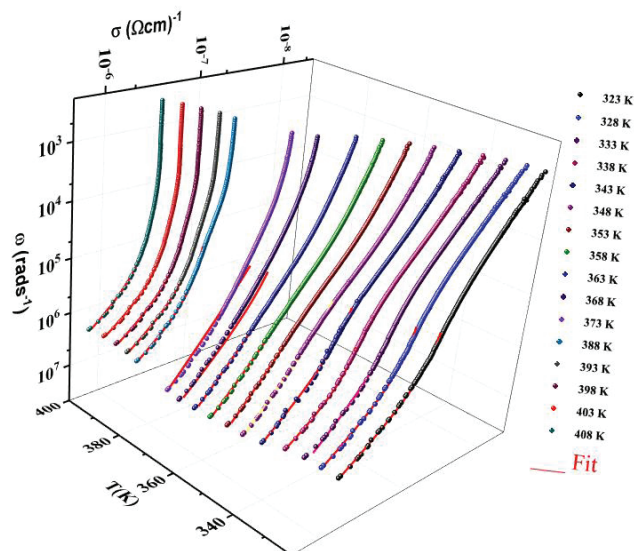

Fig. 11.   Frequency dependence of the AC conductivity at various temperatures.

region III. It is worth noticing that the variation in the activation energies values can be explained by the movement in the cationic and anionic parts. Besides, the mobility of the charge carriers is likely to result a hopping mechanism.[28]

Subsequently, a study of the ac conductivity for the sample was carried out to identify the origin of the conduction process. This makes it possible to study the transport mechanism of charge carriers as well as their interactions as a function of frequency.[29]

Figure 11 shows the evolution of the ac conductivity as a function of angular frequency. Depending on the frequencies domain, two regions are clearly distinguishable. First, we record the appearance of a plateau at a low frequency region (<0.1 MHz), which increases with temperature, reflecting the direct current conductivity σ_{dc} due to the motions of charge carriers.[30] The second regime is reported at a higher frequency (>0.1 MHz) corresponding to ac conductivity. The frequency at which the dispersion takes place is called frequency hopping.

Generally, the conductivity dispersion is analyzed using Jonsher's power law[31]:

$$\sigma_{AC}(\omega) = \sigma_{dc} + A\omega^s, \qquad (12)$$

where σ_{dc} is the direct current conductivity, A is a constant depending on temperature and s is an exponent representing the degree of interaction between mobile ions and surrounding lattices.[32]

To determine the predominant conduction mechanism of the ac conductivity for the title compound, different theoretical models correlating with the conduction mechanism of ac conductivity with the exponent s (T)[33] are used. The variation of exponent s (T), which is resulting from the fitting of the experimental data of ac conductivity, is plotted as a function

Fig. 10.   Temperature dependence of $Ln(\sigma_g T)$ versus reciprocal temperature for $[N(C_3H_7)_4]_2ZnBr_4$ compound.
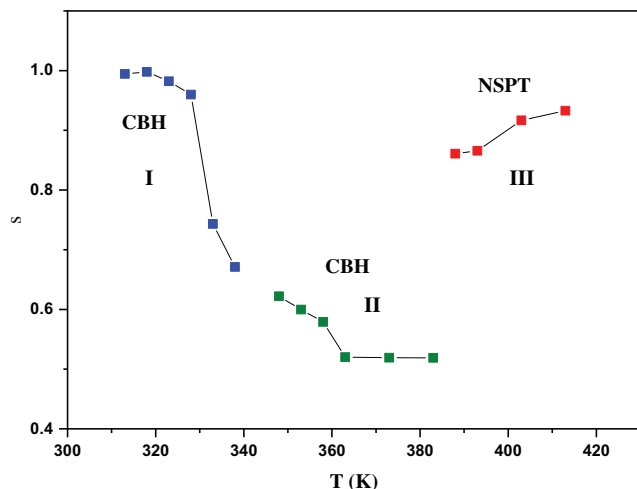
Fig. 12.   Temperature dependence of the frequency exponent *s*.

of temperature in Fig. 12. We clearly infer for this figure that the exponent s decreases with the rising temperature below and above the first phase transition (T_1 = 340 K) and increases with the increasing temperature above the second phase transition (T_2 = 393 K).

This result implies that the correlated barrier hopping (CBH) model (regions I and II) and the non-overlapping small polaron tunneling (NSPT) (region III) model stand for the most plausible models to describe the ac electrical conduction for the crystal in this range temperature.

4. Conclusion

Bis-Tetrapropylammonium tetrabromozincate with a monoclinic system ($C_{2/C}$ space group) was prepared and investigated as a function of temperature and frequency by Raman spectra. It is to be noted that the important changes in the Raman spectra are observed for some internal mode**s** of cationic parts [$N(C_3 \cdot H_7)^+$], which implies that these modes are directly connected to the phase transitions. In addition, the complex impedance analysis revealed the contribution of grains and grain boundaries to the electrical properties. In fact, a detailed analysis of the arcs demonstrated that the equivalent electrical circuit of this sample could be regarded as two elements (R//CPE) in series. Finally, the frequency-dependent (ac) conductivity was interpreted in terms of Jonscher's law. The temperature dependence of *s* was investigated to better understand the conduction mechanism in the different regions, which is attributed to the CBH model in regions (I) and (II) and the NSPT model, in region (III).

Acknowledgments

References

[1]C. Ji, S. Wang, L. Li, Z. Sun and J. Luo, The first 2D hybrid perovskite ferroelectric showing broadband white-light emission with high color rendering index, *Adv. Funct. Mater.* **29**, 1805038 (2018).

[2]X. G. Chen, Y. Zhang, D. Sun, Ji. Gao, X. Hua and W. Liao, Above room-temperature dielectric nonlinear optical switching materials based on [$(CH_3)_3S]_2[MBr_4$] (M = Cd, Mn and Zn), *Dalton Trans.* **48**, 11292 (2019).

[3]W. Li, Z. Wang, F. Deschler, S. Gao, R. Friend and A. Cheetham, Chemically diverse and multifunctional hybrid organic–inorganic perovskites, *Nat. Rev. Mater.* **2**, 16099 (2017).

[4]B. Saparov and D. Mitzi, Organic–inorganic perovskites: Structural versatility for functional materials design, *Chem. Rev.* **116**, 4558 (2016).

[5]J.-P. Correa-Baena, A. Abate, M. Saliba, W. Tress, T. Jesper Jacobsson, M. Grätzel and A. Hagfeldt, The rapid evolution efficient Pervoskite solar cells, *Energy Environ. Sci.* **10**, 710 (2017).

[6]H. Ye, Y. Tang, P. Li, W. Liao, J. Gao, X. Hua, H. Cai, P. Shi, Y. You and R. Xiong, Metal-free three-dimensional perovskite ferroelectrics, *Science* **361**, 151 (2018).

[7]Kh. Ben Brahim, M. Ben gzaiel, A. Oueslati and Gargouri, Electrical conductivity and vibrational studies induced phase transitions in [$(C_2H_5)_4$ N]FeCl$_4$, M, *RSC Adv.* **8**, 40676 (2018).

[8]R. Blachnik and Ch. Siethoff, Thermanylytical and X-ray study of some alkylammonium tetrachlorozincates, *Thermochim. Acta* **278**, 39 (1996).

[9]M. Ben Bechir, K. Karoui, K. Tababellout, K. Guidara and J. Ben Rhaeim, Alternative current conduction mechanisms of organic-inorganic compound [$N(CH_3)_3H]_2ZnCl_4$, *J. Appl. Phys.* **115**, 153708 (2014).

[10]I. Dhouib, A. Ouasri and Z. Elaoud, Disordered structures, vibrational spectroscopy, thermal behavior, and electrical properties of two new tetrachlorometallates complexes [$(CH_3CH_2CH_2)_4N]_2M^{II}Cl_4$ with M^{II} = Co and Mn, *J. Saoudi Chem. Soc.* **24**, 568 (2020).

[11]S. Chkoundali, F. Hlel and H. Khemekhem, Synthesis, crystal structure, thermal and dielectric properties of tetrapropylammonium tetrabromozincate [$N(C_3H_7)_4]_2[ZnBr_4$] compound, *J. Appl. Phys. A* **122**, 1066 (2016).

[12]N. Weslati, I. Chaabane and F. Hlel, Raman investigation of the order–disorder phase transitions in the $2[N(C_3H_7)_4]SbCl_4$ compound, *J. Vib. Spectrosc.* **81**, 90 (2015).

[13]N. Moutia, M. Ben Gzaiel, A. Oueslati and K. Khirouni, Electrical characterization and vibrational spectroscopic investigations of order-disorder phase transitions in [N ($C_3H_7)_4]_2CoCl_4$, *J. Mol. Struct.* **1134**, 697 (2017).

[14]S. Hajlaoui, I. Chaabane, A. Oueslati, K. Guidara and A. Bulou, Raman scattering investigation of the high temperature phase transition in [N ($C_3H_7)_4]_2SnCl_4$, *Spectrochim. Acta A* **136**, 547 (2015).

[15]Kh. Ben Brahim, M. Ben gzaiel, A. Oueslati, F. Hlel and M. Gargouri, Synthesis, structural characterization and electrical conduction mechanism T of the new organic–inorganic complex: [$(C_3H_7)_4N]FeCl_4$, *J. Mater. Res. Bull.* **118**, 110505 (2019).

[16]A. Ciupa-Litwa, M. Ptak, J. Hanuza, E. Kucharska and K. Beć, Comparative studies of vibrational properties and phase transitions in perovskite-like frameworks of [$(C_3H_7)_4N][M(N(CN)_2)_3$] with M = Mn, Co, Ni, *J. Raman Spectrosc.* **50**, 1561 (2019).

[17]M. Maczka, M. Ptak, A. Gagor, A. Sieradzki, P. Peksa *et al.*, Temperature- and pressure-dependent studies of a highly flexible and compressible perovskite-like cadmium dicyanamide framework templated with protonated tetrapropylamine, *J. Mater. Chem. C* **7**, 2408 (2019).

[18]H. Meekes, A. Janner and T. Janssen, Raman and infrared studies of [N $(CH_3)_4]_2ZnCl_4$, *J. Phys. B Condensed Matter* **71**, 273 (1988).

[19]P. d. R. Andradet and S. P. S. Porto, Hard core phonon frequency at transition temperature, *J. Solid State Commun.* **14**, 547 (1974).

[20]F. Jebari, P. Becker and C. Carabotos-Nédelec, Order–disorder phase transition in diethylene triammonium chlorocadmate single crystals determined by Raman spectroscopy *J. Raman Spectrosc.* **25**, 261 (1994).

[21]G. Lucazeau, Effect of pressure and temperature on Raman spectra of solids anharmonicity, *J. Raman Spectrosc.* **34**, 478 (2003).

[22]M. Oussaïd, P. Becker and C. Carabotos-Nédelec., Raman scattering investigation of order-disorder phase transitions in cadmium tris(thiourea) sulphate (CTS), *J. Raman Spectrosc.* **31**, 529 (2000).

[23]C. Carabatos-Nédelec and P. Becker, Order–disorder and structural phase transitions in solid-state materials by Raman scattering analysis, *J. Raman Spectrosc.* **28**, 663 (1997).

[24]D. Wyrzykowski, R. Kruszynski, J. Kłak, J. Mrozinski, Z. Warnke and Z. Anorg, Magnetic characteristics of tetrabutylammonium-tetrahalogenoferrates(III): X-ray crystal structure of tetrabutylammoniumtetrabromoferrate (III), *J. Allgemeine Chem.* **633**, 2071 (2007).

[25]A. Rahal, S. M. Borchani and K. Guidara. Megdiche, Electrical, dielectric properties and study of AC electrical conduction mechanism of $Li_{0.90.1}NiV_{0.5}P_{0.5}O$, M, *J. R. Soc. Open Sci.* **5,** 171472 (2018).

[26]W. Trigui, A. Oueslati, F. Hlel and A. Bulou, Raman scattering and alternative current conduction mechanism of the high-temperature phase transition in $[(C_4H_9)_4N]_3Bi_2Cl$, *J. Raman Spectrosc.* **48**, 1718 (2017).

[27]T. Rhimi, M. Toumi, K. Khirouni and S. Guermazi, AC conductivity, electric modulus analysis of $KLi(H_2PO_4)_2$ compound, correlation between the microstructure and electrical properties in high-performance $(Ba_{0.85}Ca_{0.15})(Zr_{0.1}Ti_{0.9})O_3$ lead-free piezoelectric ceramics, *J. Alloys Compd.* **714**, 546 (2017).

[28]J. Hao, W. Bai, W. Li and J. Zhai, Correlation between the microstructure and electrical properties in high-performance $(Ba_{0.85}Ca_{0.15})(Zr_{0.1}Ti_{0.9})O_3$ lead-free piezoelectric ceramics, *J. Am. Ceram. Soc.* **95**, 1998 (2012).

[29]S. Brahma, R. N. P. Choudhary and S. A. Shivashankar, Structural, thermal and electrical characterization of $NdLiMo_2O_8$ electroceramics, using impedance spectroscopy, *J. Phys. Chem. Solids* **73**, 357 (2012).

[30]E. Sentürk, Y. Koseoglu, T. Sasmaz., F. Alan and M. Tan, RC circuit and conductivity properties of $Mn_{0.6}Co_{0.4}Fe_2O_4$ nanocomposite synthesized by hydrothermal method, *J. Alloys Compd.* **578**, 90 (2013).

[31]A. Jonscher, The 'universal' dielectric response, *J. Nat.* **267**, 673 (1977).

[32]M. Ben Abdessalem, A. Aydi and N. Abdelmoula, Raman scattering, structural, electrical studies and conduction mechanism of $Ba_{0.9}$ $Ca_{0.1}$ $Ti_{0.95}$ $Zr_{0.05}$ O_3 ceramic, *J. Alloy Compd.* **774**, 685 (2019).

[33]H. Elgahami, W. Trigui, A. Oueslati and F. Hlel, Structural, thermal analysis, and electrical conductivity of new organic-inorganic $[(C_4H_9)_4P]SbCl_4$ compound, *J. Ionics* **25**, 1359 (2019).